Distributionally Robust Optimization with Data Geometry

Jiashuo Liu[1,*], **Jiayun Wu**[1,*], **Bo Li**[2] , **Peng Cui**[1,†]
[1] Department of Computer Science & Technology, Tsinghua University, Beijing, China
[2]School of Economics and Management, Tsinghua University, Beijing, China
liujiashuo77@gmail.com,jiayun.wu.work@gmail.com
libo@sem.tsinghua.edu.cn, cuip@tsinghua.edu.cn

Abstract

Distributionally Robust Optimization (DRO) serves as a robust alternative to empirical risk minimization (ERM), which optimizes the worst-case distribution in an uncertainty set typically specified by distance metrics including f-divergence and the Wasserstein distance. The metrics defined in the ostensible high dimensional space lead to exceedingly large uncertainty sets, resulting in the underperformance of most existing DRO methods. It has been well documented that high dimensional data approximately resides on low dimensional manifolds. In this work, to further constrain the uncertainty set, we incorporate data geometric properties into the design of distance metrics, obtaining our novel Geometric Wasserstein DRO (GDRO). Empowered by Gradient Flow, we derive a generically applicable approximate algorithm for the optimization of GDRO, and provide the bounded error rate of the approximation as well as the convergence rate of our algorithm. We also theoretically characterize the edge cases where certain existing DRO methods are the degeneracy of GDRO. Extensive experiments justify the superiority of our GDRO to existing DRO methods in multiple settings with strong distributional shifts, and confirm that the uncertainty set of GDRO adapts to data geometry.

1 Introduction

Machine learning algorithms with empirical risk minimization often suffer from poor generalization performance under distributional shifts in real applications due to the widespread latent heterogeneity, domain shifts, and data selection bias, *etc*. It is demanded for machine learning algorithms to achieve uniformly good performances against potential distributional shifts, especially in high-stake applications. Towards this goal, distributionally robust optimization (DRO) [32, 27, 34, 5, 17, 15], stemming from the literature of robust learning, has been proposed and developed in recent years. It optimizes the worst-case distribution within an uncertainty set $\mathcal{P}(P_{tr})$ lying around the training distribution P_{tr}. When the testing distribution P_{te} is contained in $\mathcal{P}(P_{tr})$, DRO could guarantee the generalization performance on P_{te}.

In principle, the effectiveness of DRO heavily depends on the rationality of its uncertainty set $\mathcal{P}(P_{tr})$ which is commonly formulated as a ball surrounding the training distribution endowed with a certain distance metric. An ideal uncertainty set should be constituted by all realistic distributions that may be encountered in test environments. However, existing DRO methods adopting the Wasserstein distance (i.e. WDRO methods [32, 34, 5, 17]) or f-divergence distance (i.e. f-DRO methods [27, 15]) tend to generate *over-flexible* uncertainty sets that incorporate unrealistic distributions far beyond the ideal

[*]Equal Contributions
[†]Corresponding Author

36th Conference on Neural Information Processing Systems (NeurIPS 2022).

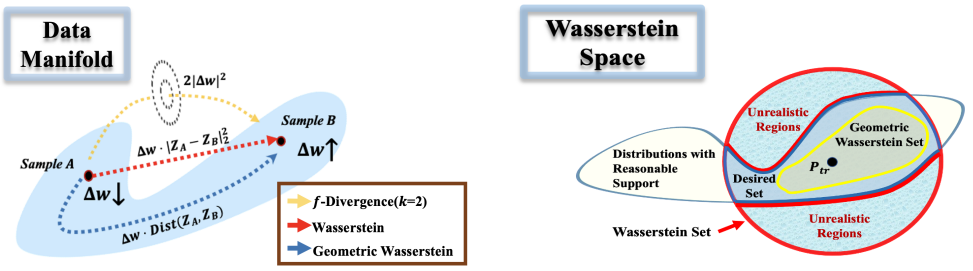

(a) Comparison of metrics on data manifold. (b) Comparison of uncertainty sets.

Figure 1: Toy illustrations. Figure (a) illustrates the transportation paths and corresponding costs of the distance metrics. (b) depicts the uncertainty set of WDRO and GDRO compared with an ideal uncertainty set in Wasserstein space, where each point denotes a distribution.

uncertainty set [19, 17]. As such unrealistic distributions must violate the underlying predicting mechanism, they are prone to be the worst-case and attract much optimization energy in the DRO framework, making the learned model deviate from the true predicting mechanism.

Here we argue that the unrealistic distributions mentioned above originate from the distance metrics' inherent ignorance of data geometry, as illustrated in Figure 1. The Euclidean-norm transportation cost measured by the L_2-Wasserstein metric leads to a straight-line transportation path as shown in Figure 1(a) (red dotted line) which deviates from the data manifold (blue region). Therefore, WDRO methods tend to create unrealistic samples beyond the underlying data manifold, resulting in unrealistic distributions. f-divergence can also be interpreted as a data geometry-independent measure of the transportation cost confined in the support of P_{tr}. Taking χ^2-divergence for example, the cost is a constant to transfer per unit of probability weights between samples, like a virtual tunnel (yellow dotted line in Figure 1(a)). In such a case, the noisy samples (e.g. outliers or samples with label noises) are more prone to be the worst-case and thus gather much larger weights than normal samples. The resultant distribution is obviously unrealistic.

To mitigate the problem, it is imperative to introduce a new distance metric incorporating data geometry to further constrain the uncertainty set and avoid the undesired cases. As illustrated in Figure 1(a), considering the common assumption that data lie on a low-dimensional manifold [29, 35, 2], we expect the probability density transportation path (the blue dotted line) is *restricted within the data manifold* (the blue region). In this way, the uncertainty set (i.e. the Geometric Wasserstein Set as shown in Figure 1(b)) could inherently exclude the distributions beyond the data manifold. Furthermore, it is harder to gather probability weights on isolated noisy samples, which also mitigate the undesired cases in f-DRO.

In this work, we propose a novel Geometric Wasserstein DRO (GDRO) method by exploiting the discrete Geometric Wasserstein distance [7] which measures the transportation cost of probability density along the geodesic in a metric space. As the Geometric Wasserstein distance does not enjoy an analytical expression, we derive an approximate algorithm from the Gradient Flow in the Finsler manifold endowed with Geometric Wasserstein Distance (in section 3.2). We further theoretically specify an exponentially vanishing error rate of our approximation as well as a $O(1/\sqrt{T})$ convergence rate of our algorithm, and characterize the edge cases where GDRO will degenerate to f-DRO or Wasserstein DRO (in section 3.3 and 3.4). Comprehensive experiments encompassing various distributional shifts, including sub-population shifts and class difficulty shifts, validate the effectiveness of our proposed GDRO (in section B). We also observe a lower Dirichlet Energy (i.e. higher smoothness) of GDRO's estimated worst-case distribution w.r.t the data manifold compared with existing DRO methods, justifying its adaptability to data geometry.

2 Preliminaries on Distributionally Robust Optimization

Notations. $X \in \mathcal{X}$ denotes the covariates, $Y \in \mathcal{Y}$ denotes the target, $f_\theta(\cdot) : \mathcal{X} \to \mathcal{Y}$ is the predictor parameterized by $\theta \in \Theta$. $P_{tr}(X, Y)$ and $P_{te}(X, Y)$ abbreviated with P_{tr} and P_{te} respectively represent the joint training distribution and test distribution. The random variable of data points is denoted by $Z = (X, Y) \in \mathcal{Z}$.

Distributionally Robust Optimization (DRO) is formulated as:

$$\theta^* = \arg\min_{\theta\in\Theta} \sup_{P\in\mathcal{P}(P_{tr})} \mathbb{E}_P[\ell(f_\theta(X), Y)], \tag{1}$$

where ℓ is a loss function, $\mathcal{P}(P_{tr}) = \{P : \textit{Dist}(P, P_{tr}) \leq \epsilon\}$ characterizes the uncertainty set surrounding the training distribution restricted by a radius ϵ, and *Dist* is a distance metric between probability distributions. Most works specify the *Dist* metric as the f-divergence [27, 15] or the Wasserstein distance [32, 34, 5, 31, 16].

f-divergence DRO (*abbr.* f-DRO) f-divergence is defined as $D_f(P\|Q) = \int f(dP/dQ)dQ$, where $f(\cdot)$ is a convex function and $f(1) = 0$. Two typical instances of f-divergences are KL-divergence ($f(t) = t\log t$) and χ^2-divergence ($f(t) = (t-1)^2$). [27] theoretically demonstrates the equivalence between χ^2-DRO and the variance-regularized empirical risk minimization (ERM) problem, and [15] derives the optimization algorithm for a family of f-DRO. However, as proven in [19], f-DRO faces the over-pessimism problem and ends up giving a classifier only fitting the given training distribution, which we attribute to the ignorance of data geometry. As shown in Figure 1(a), f-divergence only cares about the probability of each sample (only dP, dQ occur). However, data geometry information is crucial for a reasonable uncertainty set, since it is well-accepted that data lie on a low-dimensional manifold and adjacent data points have similar degrees of importance. For example, for heterogeneous data, while one hopes to focus on some sub-population (e.g., put more weights on a group of data), without data geometric information, the distribution in the f-divergence ball is prone to only focus on some isolated samples with higher noises (as shown in Figure 5(a)). And in Figure 5(b), we find the worst-case distribution of f-DRO (with KL-divergence) is not smooth (with larger Dirichlet Energy) w.r.t. the data manifold.

Wasserstein DRO (*abbr.* WDRO) Compared with the f-divergence ball that does not extend the support of the training distribution, the uncertainty set built with Wasserstein distance allows for the extension of the support [32, 34, 5]. [31, 16, 5] convert the original problem into a regularized ERM problem, but it is suitable only for a limited class of loss functions and transportation cost functions. [34] proposes an approximate optimization method for Wasserstein DRO that could be applied to deep neural networks, which protects models from adversarial attacks. However, the flexibility of the Wasserstein ball also causes an over-pessimistic estimation under strong distributional shifts [17], where the created samples are too noisy to obtain a confident model. As demonstrated in Figure 5(a), WDRO adds much more noises to the data and thus hurts the generalization performances in practice.

Therefore, to mitigate the over-pessimism problem of DRO, we propose to incorporate the geometric properties into the uncertainty set. Compared with traditional shape-constrained methods [21, 20] for multivariate extreme event analysis that use the unimodality to constitute the uncertainty set, our proposed method characterizes the data manifold in a data-driven way and incorporates it into the DRO framework intrinsically via the Geometric Wasserstein distance metric, which is also compatible with manifold learning and graph learning methods.

3 Proposed Method

In this work, we propose Distributionally Robust Optimization with Geometric Wasserstein distance (GDRO). In the following of this section, we first introduce the Geometric Wasserstein distance and propose the overall objective of GDRO; then we derive an approximate algorithm for optimization utilizing Gradient Flow; finally, some theoretical properties are proved and connections with existing DRO methods are demonstrated.

3.1 Discrete Geometric Wasserstein Distance $\mathcal{GW}_{G_0}$ and GDRO

We firstly introduce the Discrete Geometric Wasserstein distance, which extends the Benamou-Brenier formulation of the optimal transport problem to a metric space. The first step is to define a discrete velocity field and its discrete divergence, which we mainly follow the construction by Chow *et al.* [7].

Consider a given weighted finite graph $G_0 = (V, E, w)$ with n nodes, where $V = \{1, 2, \ldots, n\}$ is the vertex set, E is the edge set and $w = (w_{ij})_{i,j\in V}$ is the weight of each edge. A *velocity field* $v = (v_{ij})_{i,j\in V} \in \mathbb{R}^{n\times n}$ on G_0 is defined to be a skew-symmetric matrix on the edge set E such that $v_{ij} = -v_{ji}$ if $(i, j) \in E$. The probability set (simplex) $\mathscr{P}(G_0)$ supported on V is defined as $\mathscr{P}(G_0) = \{(p_i)_{i=1}^n \in \mathbb{R}^n | \sum_{i=1}^n p_i = 1, p_i \geq 0, \text{for any } i \in V\}$ and its interior

is denoted by $\mathscr{P}_o(G_0)$. κ_{ij} is a predefined "cross-sectional area" typically interpolated with the associated nodes' densities p_i, p_j. The direct approach is to take the arithmetic average such that $\kappa_{ij}(p) = (p_i + p_j)/2$. However, to ensure the positiveness of p during optimization, we adopt the *upwind interpolation*:$\kappa_{ij}(p) = \mathbb{I}(v_{ij} > 0)p_j + \mathbb{I}(v_{ij} \leq 0)p_i$. One could thereafter define the product $pv \in \mathbb{R}^{n\times n}$, called *flux function* on G_0, by $pv := (v_{ij}\kappa_{ij}(p))_{(i,j)\in E}$. The *divergence* of pv is $\mathrm{div}_{G_0}(pv) := -(\sum_{j\in V:(i,j)\in E} \sqrt{w_{ij}} v_{ij}\kappa_{ij}(p))_{i=1}^n$ which is a vector in $\mathbb{R}^n$. The divergence vector is supposed to lie in the tangent space of $\mathscr{P}_o(G_0)$, summing over all the in-fluxes and out-fluxes along edges of a certain node, with each edge transporting a probability density $\sqrt{w_{ij}} v_{ij}\kappa_{ij}(p)$. Now we are ready to define Geometric Wasserstein distance in Equation 2.

Definition 3.1 (Discrete Geometric Wasserstein Distance $\mathcal{GW}_{G_0}(\cdot,\cdot)$ [7])**.** *Given a finite graph G_0, for any pair of distributions $p^0, p^1 \in \mathscr{P}_o(G_0)$, define the Geometric Wasserstein Distance:*

$$\mathcal{GW}^2_{G_0}(p^0, p^1) := \inf_v \left\{ \int_0^1 \frac{1}{2} \sum_{(i,j)\in E} \kappa_{ij}(p) v_{ij}^2 dt : \frac{dp}{dt} + div_{G_0}(pv) = 0, p(0) = p^0, p(1) = p^1 \right\}, \quad (2)$$

where $v \in \mathbb{R}^{n\times n}$ denotes the velocity field on G_0, p is a continuously differentiable curve $p(t) : [0,1] \to \mathscr{P}_o(G_0)$, and $\kappa_{ij}(p)$ is a pre-defined interpolation function between p_i and p_j.

Intuitively v is a velocity field continuously transporting masses to convert the density distribution from p^0 to p^1 along a curve in the Wasserstein space [36]. Equation 2 measures the shortest (geodesic) length among all possible plans, which is calculated by integrating a total "kinetic energy" of the velocity field over the transportation process. Compared with the Benamou-Brenier formulation of continuous L_2-Wasserstein distance, it ensures that the transportation path *stays within the manifold* (as the blue dotted line shown in Figure 1(a)), and it induces a smoother estimate of the worst-case probability distribution w.r.t the data structure since weights are exchanged just between neighbors.

Then we present the *overall objective function* of Distributionally Robust Optimization with Geometric Wasserstein distance (GDRO). Given the training dataset $D_{tr} = \{(x_i, y_i)\}_{i=1}^n$ and its empirical marginal distribution $\hat{P}_{tr} = \frac{1}{n}\sum_i \delta(x_i)$, along with a manifold structure represented by graph G_0, we intend to obtain a distributionally robust predictor parameterized by θ^* such that for certain $\epsilon > 0$:

$$\theta^* = \arg\min_{\theta\in\Theta} \sup_{P:\mathcal{GW}^2_{G_0}(\hat{P}_{tr},P)\leq\epsilon} \left\{ \mathcal{R}_n(\theta, p) = \sum_{i=1}^n p_i \ell(f_\theta(x_i), y_i) - \beta \sum_{i=1}^n p_i \log p_i \right\}. \quad (3)$$

We add a minor entropy-regularization with a small β as proposed in the entropy-balancing literature [18] to avoid singular cases and ensure the convergence of our optimization in section 3.2. Owing to the Geometric Wasserstein distance, the uncertainty set of GDRO excludes those distributions supported on points beyond the data manifold and the Geometric Wassserstein Ball is directional in Wasserstein space as it stretches along the data structure, as depicted in Figure 1(b).

How is G_0 estimated? To characterize the data manifold, the G_0 used in GDRO is constructed as a k-nearest neighbor (kNN) graph *from the training data only*, as the kNN graph is shown to have a good approximation of the geodesic distance within local structures on the manifold [25, 9]. Note that our GDRO is *compatible with any manifold learning and graph learning methods*.

3.2 Optimization

In this subsection, we derive the optimization algorithm for GDRO. Due to the lack of an analytical form of the Geometric Wasserstein distance, we give up providing a prescribed amount ϵ of robustness

Algorithm 1 Geometric Wasserstein Distributionally Robust Optimization (GDRO)

Input: Training Dataset $D_{tr} = \{(x_i, y_i)\}_{i=1}^n$, learning rate α_θ, gradient flow iterations T, entropy term β, manifold representation G_0 (learned by kNN algorithm from D_{tr}).

Initialization: Sample weights initialized as $(1/n, \ldots, 1/n)^T$. Predictor's parameters initialized as $\theta^{(0)}$.

for $i = 0$ **to** Epochs **do**

1. Simulate gradient flow for T time steps according to Equation 5$\sim$18 to learn an approximate worst-case probability weight p^T.
2. $\theta^{(i+1)} \leftarrow \theta^{(i)} - \alpha_\theta \nabla_\theta(\sum_i p_i^T \ell_i(\theta))$

end for

in Equation 3 and propose an alternate optimization algorithm as an approximation. For fixed probability weights p, the parameter θ could be optimized via gradient descents for $\mathcal{R}_n(\theta, p)$ w.r.t. θ in parameter space Θ. The inner supremum problem can be approximately solved via gradient ascents for $\mathcal{R}_n(\theta, p)$ w.r.t. p in the *Geometric Wasserstein space* $(\mathscr{P}_o(G_0), \mathcal{GW}_{G_0})$. And the cost measured by $\mathcal{GW}^2_{G_0}(\hat{P}_{tr}, \cdot)$ could be approximated with the length of the gradient flow, which is a curve in $(\mathscr{P}_o(G_0), \mathcal{GW}_{G_0})$.

Here we clarify some notations. $p : [0, T] \mapsto \mathscr{P}_o(G_0)$ denotes the *continuous gradient flow*, and the probability weight of the i-th sample at time t is abbreviated as $p_i(t)$. The *time-discretized gradient flow* corresponding with the time step τ is denoted as $\hat{p}_\tau : [0, T] \mapsto \mathscr{P}_o(G_0)$, and $\hat{p}_\tau(t)$ is abbreviated as $\hat{p}^t_\tau$. For the optimization, we adopt the time-discretized definition of Gradient Flow [36] for $-\mathcal{R}_n(\theta, p)$ in the Geometric Wasserstein space $(\mathscr{P}_o(G_0), \mathcal{GW}_{G_0})$ as: (with the time step τ)

$$\hat{p}_\tau(t + \tau) = \arg \max_{p \in \mathscr{P}_o(G_0)} \mathcal{R}_n(\theta, p) - \frac{1}{2\tau} \mathcal{GW}^2_{G_0}(\hat{p}_\tau(t), p). \tag{4}$$

When $\tau \to 0$, the time-discretized gradient flow $\hat{p}_\tau$ becomes the continuous one p. Note that Equation 4 describes the Gradient Flow as a steepest ascent curve locally optimizing for a maximal objective within an infinitesimal Geometric Wasserstein ball, and it coincides with the Lagrangian penalty problem of Equation 3. In theorem 3.1 we would prove that Equation 4 finds the exact solution to a *local* GDRO at each time step.

Following Chow *et al.* [7], the analytical solution to Equation 4 as $\tau \to 0$ could be derived as:

$$\frac{dp_i}{dt} = \sum_{j:(i,j)\in E} w_{ij}\kappa_{ij}(\ell_i - \ell_j) + \beta \sum_{j:(i,j)\in E} w_{ij}\kappa_{ij}(\log p_j - \log p_i), \tag{5}$$

where p_i denotes the time-dependent probability function of the i-th sample, l_i denotes the loss of the i-th sample and we take an upwind interpolation of κ: $\kappa_{ij}(p) = \mathbb{I}(v_{ij} > 0)p_j + \mathbb{I}(v_{ij} \leq 0)p_i$, so that the probability density transferred on an edge equals the density from the origin node associated with the velocity field. The upwind interpolation guarantees that the probability weight p stays positive along the Gradient Flow in Equation 5. Then we discretize equation 5 with Forward Euler Method:

$$p_i(t + \alpha) = p_i(t) + \alpha dp_i(t)/dt, \tag{6}$$

where α is a learning rate. For our algorithm, we control the maximum time step as $t \leq T$ in Equation 18 to approximately restrict the radius of the Geometric Wasserstein ball. We prove in theorem 3.2 that for the final time step $t = T$, the probability weights $p(T)$ learned by Equation 18 guarantees a *global* error rate e^{-CT} from the worst-case risk $\mathcal{R}_n(\theta, p^*)$ constrained in an $\epsilon(\theta)$-radius ball where $\epsilon(\theta) = \mathcal{GW}^2_{G_0}(\hat{P}_{tr}, p(T))$ and $p^* = \arg\sup_p\{\mathcal{R}_n(\theta, p) : \mathcal{GW}^2_{G_0}(\hat{P}_{tr}, p) \leq \epsilon(\theta)\}$. The result is similar to conventions in WDRO [34], which gives up providing a prescribed radius of its uncertainty set but turns to an approximation with a intermediate hyperparameter. Pseudo-code of the whole algorithm is shown in Algorithm 1. The whole derivations are in Appendix.

3.3 Theoretical Properties

In this section, we prove the equivalence between our Gradient-Flow-based algorithm and a local GDRO problem, and the bound of its global error rate as well as the convergence rate is derived. We first provide the robustness guarantee for the Lagrangian penalty problem in Equation 4.

Theorem 3.1 (Local Robustness Guarantees of Lagrangian Penalty Problem)**.** *For any $\tau > 0, t > 0$ and given θ, denote the solution of Equation 4 as $p^*(\theta) = \arg\sup_{p\in\mathscr{P}(G_0)} \mathcal{R}_n(\theta, p) - \frac{1}{2\tau}\mathcal{GW}^2_{G_0}(\hat{p}^t_\tau(\theta), p)$. Let $\epsilon_\tau(\theta) = \mathcal{GW}^2_{G_0}(\hat{p}^t_\tau(\theta), p^*(\theta))$, we have*

$$\sup_{p\in\mathscr{P}_o(G_0)} \mathcal{R}_n(\theta, p) - \frac{1}{2\tau}\mathcal{GW}^2_{G_0}(\hat{p}^t_\tau(\theta), p) = \sup_{p:\mathcal{GW}^2_{G_0}(\hat{p}^t_\tau(\theta),p)\leq\epsilon_\tau(\theta)} \mathcal{R}_n(\theta, p). \tag{7}$$

Theorem 3.1 proves that at each time step our Lagrangian penalty problem is equivalent to a local GDRO within the $\epsilon_\tau(\theta)$-radius Geometric Wasserstein ball. It further shows that with $\tau \to 0$ in Equation 4, our gradient flow constantly finds the steepest descent direction. Then we theoretically analyze the global error rate brought by our approximate algorithm.

Theorem 3.2 (Global Error Rate Bound)**.** *Given the model parameter θ, denote the approximate worst-case by gradient descent in Equation 18 after time t as $p^t(\theta)$, and $\epsilon(\theta) = \mathcal{GW}^2_{G_0}(\hat{P}_{tr}, p^t(\theta))$ denotes the distance between our approximation p^t and the training distribution $\hat{P}_{tr}$. Then denote*

the real worst-case distribution within the $\epsilon(\theta)$-radius discrete Geometric Wasserstein-ball as $p^*(\theta)$, that is,

$$p^*(\theta) = \arg \sup_{p:\mathcal{GW}^2_{G_0}(\hat{P}_{tr},p)\leq\epsilon(\theta)} \sum_{i=1}^{n} p_i \ell_i - \beta \sum_{i=1}^{n} p_i \log p_i. \tag{8}$$

Here we derive the bound w.r.t. the error ratio of objective function $R_n(\theta, p)$ (abbr. $\mathcal{R}(p)$). For $\theta \in \Theta$, there exists $C > 0$ such that

$$\textit{Error Rate} = \left(\mathcal{R}(p^*) - \mathcal{R}(p^t)\right) / \left(\mathcal{R}(p^*) - \mathcal{R}(\hat{P}_{tr})\right) < e^{-Ct}, \tag{9}$$

and when $t \to \infty$, Error Rate $\to 0$. The value of C depends on ℓ, β, n.

Theorem 3.2 theoretically characterizes 'how far' our approximation p^t is from the real worst-case p^* in terms of the drop ratio of the objective function $\mathcal{R}(p)$. At last we derive the convergence rate of our Algorithm 1.

Theorem 3.3 (Convergence of Algorithm 1)**.** *Denote the objective function for the predictor as:*

$$F(\theta) = \sup_{\mathcal{GW}^2_{G_0}(\hat{P}_{tr},p)\leq\epsilon(\theta)} \mathcal{R}_n(\theta, p), \tag{10}$$

which is assumed as L-smooth and $\mathcal{R}_n(\theta, p)$ satisfies L_p-smoothness such that $\|\nabla_p \mathcal{R}_n(\theta, p) - \nabla_p \mathcal{R}_n(\theta, p')\|_2 \leq L_p \|p - p'\|_2$. $\epsilon(\theta)$ follows the definition in Theorem 3.2. Take a constant $\Delta_F \geq F(\theta^{(0)}) - \inf_\theta F(\theta)$ and set step size as $\alpha = \sqrt{\Delta_F/(LK)}$. For $t \geq T_0$ where T_0 is a constant, denote the upper bound of $\|p^t - p^*\|_2^2$ as γ and train the model for K steps, we have:

$$\frac{1}{K}\mathbb{E}\left[\sum_{k=1}^{K} \|\nabla_\theta F(\theta^{(k)})\|_2^2\right] - \frac{(1 + 2\sqrt{L\Delta_F/K})}{1 - 2\sqrt{L\Delta_F/K}} L_p^2 \gamma \leq \frac{2\Delta_F}{\sqrt{\Delta_F K} - 2L\Delta_F}. \tag{11}$$

Here we make a common assumption on the smoothness of the objective function as in [34]. As $K \to \infty$, $\nabla_\theta F(\theta^{(k)})$ will achieve a square-root convergence only if γ is controlled by the exponentially vanishing error rate in Theorem 3.2. And the accuracy parameter γ remains a fixed effect on optimization accuracy.

3.4 Connections with Conventional DRO Methods

In Theorem 3.4, we illustrate the connections of our GDRO with f-DRO.

Theorem 3.4 (Connection with f-DRO with KL-diveregence (KL-DRO).)**.** *Relax the discrete Geometric Wasserstein-ball regularization (set $\epsilon \to \infty$) and set the graph G_0 to a fully-connected graph, and then the solution of GDRO is equivalent to the following form of KL-DRO:*

$$\min_{\theta\in\Theta} \sup_{p:D_{KL}(p\|\hat{P}_{tr})\leq\hat{\epsilon}(\theta)} \sum_{i=1}^{n} p_i \ell(f_\theta(x_i), y_i), \quad \textit{with } \hat{\epsilon}(\theta) = D_{KL}(p^*(\theta)\|\hat{P}_{tr}), \tag{12}$$

where $p^*(\theta) = \arg\max_p \sum_{i=1}^n p_i \ell(f_\theta(x_i), y_i) - \beta \sum_{i=1}^n p_i \log p_i$.

Remark (Connections with WDRO)**.** *Since conventional WDRO allows distributions to extend training support, our proposed GDRO is intrinsically different from WDRO. Intuitively, for infinite samples, if the graph G_0 is set to a fully-connected graph with edge weights $w_{ij} = \|z_i - z_j\|^2$ and β is set to 0, our GDRO resembles support-restricted version of WDRO.*

4 Experiments

In this section, we investigate the empirical performance of our proposed GDRO on different simulation and real-world datasets under various kinds of distributional shifts, including *sub-population shifts* and *class difficulty shifts*. As for baselines, we compare with empirical risk minimization (ERM), WDRO [5, 34] and two typical f-DRO methods [15], including KL-DRO ($f(t) = t \ln t$) and χ^2-DRO ($f(t) = (t-1)^2$).

Implementation Details For all experiments, G_0 is constructed as a k-nearest neighbor graph from the *training data only* at the initialization step. Specifically, we adopt NN-Descent [14] to efficiently estimate the k-nearest neighbor graph for the large-scale dataset Colored MNIST while performing

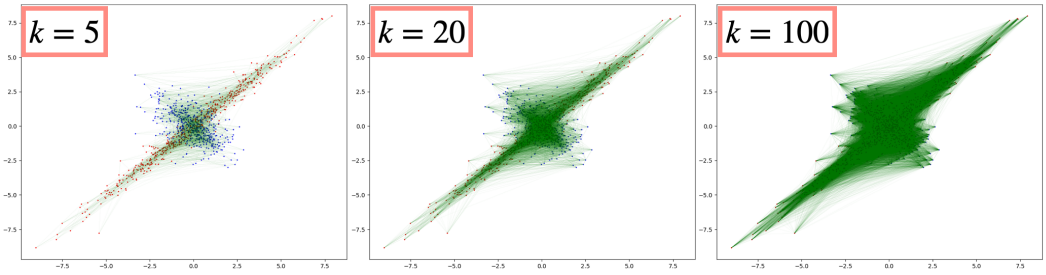

Figure 2: Visualization of learned kNN graph with different k of the regression data, which is projected on the plane spanned by the unit vector of V axis and θ_S with a projection matrix $\begin{bmatrix} \mathbf{0}_{1,5} & \mathbf{0}_{1,4} & 1 \\ \theta_S^T & \mathbf{0}_{1,4} & 0 \end{bmatrix}$.

an exact search for k-nearest neighbors in the other experiments. We adopt MSE as the empirical loss function for regression tasks and cross-entropy for classification tasks. We use MLPs for the Colored MNIST and Ionosphere datasets, and linear models in the other experiments. Besides, we find that the two-stage optimization is enough for good performances, as mentioned in [23], and we use it in our experiments. Note that GDRO is *compatible with any parameterized models including deep models*. The simulation of gradient flow in Equation 18 is implemented by message propagation with DGL package [38], which scales linearly with sample size and enjoys parallelization by GPU.

4.1 Simulation Data

In this subsection, we use simulations to verify that our GDRO could deal with sub-population shifts and to some extent resist the label noises. And we also visualize the effects of the kNN algorithm as well as the sensitivity of GDRO to the parameter k.

Table 1: Results on the Selection Bias Experiments. We report the root mean square errors.

Simulation 1: regression data without label noises									
	Train(major)	Train(minor)			Test				Parameter
Bias Ratio r	$r = 1.9$	$r = -1.3$	$r = -1.5$	$r = -1.7$	$r = -1.9$	$r = -2.3$	$r = -2.7$	$r = -3.0$	Est Error
ERM	**0.339**	0.876	0.892	0.884	0.864	0.880	0.843	0.888	0.423
WDRO	**0.339**	0.877	0.894	0.885	0.865	0.882	0.844	0.890	0.424
χ^2-DRO	0.411	0.744	0.757	0.741	0.733	0.742	0.714	0.755	0.367
KL-DRO	0.370	0.713	0.728	0.716	0.708	0.713	0.685	0.724	0.319
GDRO	0.493	**0.492**	**0.508**	**0.489**	**0.501**	**0.483**	**0.486**	**0.496**	**0.033**
Simulation 2: regression data with label noises									
ERM	**0.335**	0.845	0.885	0.879	0.874	0.884	0.882	0.876	0.422
WDRO	**0.335**	0.896	0.887	0.880	0.875	0.886	0.884	0.877	0.423
χ^2-DRO	0.375	0.866	0.855	0.856	0.843	0.860	0.854	0.845	0.408
KL-DRO	0.393	0.879	0.868	0.866	0.856	0.876	0.866	0.861	0.391
GDRO	0.542	**0.537**	**0.553**	**0.549**	**0.534**	**0.539**	**0.555**	**0.550**	**0.058**
Simulation 3: vary k under Simulation 1									
GDRO ($k = 5$)	0.493	0.492	0.508	0.489	0.501	0.483	0.486	0.496	0.033
GDRO ($k = 20$)	0.518	0.507	0.521	0.502	0.514	0.497	0.504	0.508	0.036
GDRO ($k = 100$)	0.379	0.673	0.688	0.676	0.670	0.672	0.647	0.683	0.286

1. Regression: Sub-population Shifts via Selection Bias Mechanism

Data Generation The input features $X = [S, U, V]^T \in \mathbb{R}^{10}$ are comprised of stable features $S \in \mathbb{R}^5$, noisy features $U \in \mathbb{R}^4$ and the spurious feature $V \in \mathbb{R}$:

$$S \sim \mathcal{N}(0, 2\mathbb{I}_5) \in \mathbb{R}^5, \quad U \sim \mathcal{N}(0, 2\mathbb{I}_4) \in \mathbb{R}^4, \quad Y = \theta_S^T S + 0.1 \cdot S_1 S_2 S_3 + \mathcal{N}(0, 0.5), \tag{13}$$

$$V \sim \text{Laplace}(\text{sign}(r) \cdot Y, \ \frac{1}{5 \ln |r|}) \in \mathbb{R}, \tag{14}$$

where $\theta_S \in \mathbb{R}^5$ is the coefficient of the true model. $|r| > 1$ is a factor for each sub-population. S are *stable features* with the invariant relationship with Y. U are *noisy features* such that $U \perp Y$. And V is the *spurious feature* whose relationship with Y is unstable and is controlled by the factor r. Intuitively, $\text{sign}(r)$ controls whether the spurious correlation between V and Y is positive or negative. And $|r|$ controls the strength of the spurious correlation: the larger $|r|$ is, the stronger the spurious correlation is.

Simulation Setting 1 In training, we generate 10000 points, where the major group contains 95% data with $r = 1.9$ (i.e. strong positive spurious correlation) and the minor group contains 5% data with $r = -1.3$ (i.e. weak negative spurious correlation). As shown in Figure 2, the training data is the union of two sub-spaces. In testing, we vary $r \in \{-1.5, -1.7, -1.9, -2.3, -2.7, -3.0\}$ to simulate stronger negative spurious correlations between V and Y. Notably, the testing data also lie on the same manifold as the training. We use the *linear model* and calculate the root-mean-square errors (RMSE) and the parameter estimation errors Est Error $= \|\hat{\theta} - \theta^*\|_2$ of different methods ($\theta^* = [\theta_S, 0, \ldots, 0]^T$). The results are shown in the *Simulation 1* in Table 7.

Simulation Setting 2 Then to test whether GDRO could resist label noises, we randomly sample 20 points and add label noises to them via $\tilde{Y} = Y + \text{Std}(Y)$ where std(Y) denotes the standard derivation of the marginal distribution of Y. The results are shown in the *Simulation 2* in Table 7. And we visualize the learned worst-case distribution of three methods in Figure 5(a) and 5(b).

Analysis **(1)** From the results of *Simulation 1* and *Simulation 2* in Table 7, GDRO outperforms all the baselines in terms of low prediction error on the minor group under different strengths of spurious correlations. **(2)** From *Simulation 2* in Table 7, compared with KL-DRO and χ^2-DRO, GDRO is only slightly affected by the label noises. Also, from Figure 5(a), compared with GDRO, KL-DRO puts much heavier weights on the noisy points (red points of f-DRO are much larger). And GDRO focuses more on the minor group (blue points), which results in their different performances under *Simulation 2*. Further, to investigate this phenomenon, we quantify the smoothness via Dirichlet Energy. In Figure 5(b), we plot the Dirichlet Energy w.r.t the relative entropy $KL(\hat{P}\|\hat{P}_{tr})$ between the learned distribution $\hat{P}$ and training distribution $\hat{P}_{tr}$, which proves that the learned weights of GDRO are much smoother w.r.t. the data manifold. And this property helps GDRO to resist the label noises, since GDRO does not allow extremely high weights on the isolated points. **(3)** The third sub-figure in Figure 5(a) verifies our analysis on WDRO that it introduces much more label noises (red points).

Discussion on kNN To test whether GDRO is sensitive to the parameter k of the kNN graph G_0, we vary $k \in \{5, 20, 100\}$ and test the performances of our GDRO under *simulation setting 1*. We also visualize the kNN graphs in Figure 2, which show that kNN consistently manages to fit the data manifold well until $k = 100$. And empirical results of *Simulation 3* in Table 7 prove that with $k < 100$, GDRO performs stably better than the baselines with small and moderate k, except that smaller k leads to slower convergence since sparse graphs restrain the flow of probability weights. Still, we present an extreme *failure case* where KNN achieves a poor approximation of the data manifold. When k increases to an extremely large number as $k = 100$, the neighborhood of kNN diffuses and two manifolds start to merge on the graph, in which case GDRO could not distinguish between two sub-populations and its performance degrades as shown in the Table 7. Actually, in Theorem 3.4 of this paper, we have proved that with an infinitely large k, GDRO could be reduced to KL-DRO, which completely ignores data geometry. Still, we have to clarify that kNN and GDRO perform stably well for a large range of k.

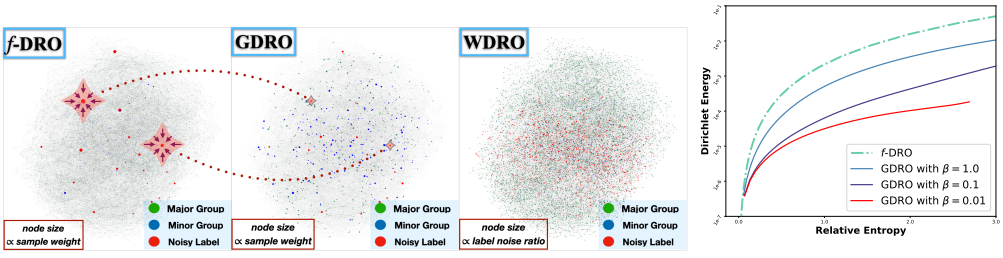

(a) Visualization of learned weights of f-DRO and GDRO. (b) Weight smoothness.

Figure 3: Explanatory studies of *Simulation 2* for the regression data. **Figure (a)** visualizes the learned worst-case distribution of f-DRO, GDRO, and WDRO on kNN, and the size of each node is proportional to its sample weight or its label noise ratio. **Figure (b)** plots the Dirichlet Energy w.r.t the relative entropy, which measures the smoothness of learned weights given the same $D_{KL}(p\|\hat{P}_{tr})$.

2. Classification: Sub-population Shifts with High-dimensional Manifold Data

Data Generation In this setting, data are high-dimensional but with a low-dimensional structure. The data generation is similar to [30] and is a typical classification setting in OOD generalization.

We introduce the spurious correlation between the label $Y = \{+1, -1\}$ and the spurious attribute $A = \{+1, -1\}$. We firstly generate low-dimensional data $X_{low} = [S, V]^T \in \mathbb{R}^{10}$ as:

$$S \sim \mathcal{N}(Y\mathbf{1}, \sigma_s^2 \mathbb{I}_5), \quad V \sim \mathcal{N}(A\mathbf{1}, \sigma_v^2 \mathbb{I}_5), \quad \text{where } A = \begin{cases} Y, \text{with probability } r, \\ -Y, \text{with probability } 1-r. \end{cases} \tag{15}$$

Intuitively, $r \in [0, 1]$ tunes the proportions of sub-populations and controls the spurious correlation between A and Y. When $r > 0.5$, the spurious attribute A is positively correlated with Y; and when $r < 0.5$, the spurious correlation becomes negative. And larger $|r - 0.5|$ results in stronger spurious correlation between A and Y. Then to convert the low-dimensional data to high-dimensional space, X_{low} is multiplied by a column full rank matrix H as:

$$X_{high} = (HX_{low}) \in \mathbb{R}^{300}, \tag{16}$$

where $H \in \mathbb{R}^{300 \times 10}$ is full column rank, and we randomly choose H in each run.

Simulation Setting For both the training and testing data, we set $\sigma_s^2 = 1.0$ and $\sigma_v^2 = 0.3$. We use *linear models* with cross-entropy loss for all methods. In training, we set $r = 0.85$ (A is positively correlated with Y). In testing, we design two environments with $r_1 = 0.5$ ($A \perp Y$) and $r_2 = 0.0$ (A is negatively correlated with Y) to introduce distributional shifts. Apart from the natural setting without label noises, we also test the performances under label noises. Specifically, we add 4% label noises in the training data by flipping the label Y. We run the experiments 10 times, each time with one random matrix H. We report the mean accuracy in Table 6.

Analysis From the results in Table 6, our GDRO outperforms all baselines under the sub-population shifts, and it is not affected much by the label noises, which validates the effectiveness of our GDRO.

4.2 Real-World Data

We evaluate our method on four real-world datasets. Due to space limits, we place two of them here, with various kinds of distributions, including sub-populations shifts and class difficulty shifts, and the others can be found in Appendix. We use MLPs with cross-entropy loss in these experiments.

Colored MNIST: Sub-population Shifts & Label Noises Following Arjovsky *et al.* [1], Colored MNIST is a binary classification task constructed on the MNIST dataset. Firstly, a binary label Y is assigned to each image according to its digit: $Y = 0$ for digit $0 \sim 4$ and $Y = 1$ for digit $5 \sim 9$. Secondly, we induce noisy labels $\tilde{Y}$ by randomly flipping the label Y with a probability of 0.2. Then we sample the color id C spuriously correlated with $\tilde{Y}$ as $C = \begin{cases} +\tilde{Y}, & \text{with probability } 1-r, \\ -\tilde{Y}, & \text{with probability } r. \end{cases}$

Intuitively, r controls the spurious correlation between Y and C. When $r < 0.5$, C is positively correlated with Y; and when $r > 0.5$, the spurious correlation becomes negative. And $|r - 0.5|$ controls the strength of the spurious correlation. In *training*, we randomly sample 5000 data points and set $r = 0.85$ (*strong negative* spurious correlation between C and Y) and in *testing*, we set $r = 0$ (*strong positive* spurious correlation), inducing strong shifts between training and testing. Results are shown in Table 8.

Ionosphere Radar Classification: Class Difficulty Shifts Ionosphere Radar Dataset [11] consists of return signals from the ionosphere of a phased array radar system in Google Bay, Labrador. The electromagnetic signals were processed by an auto-correlation function to produce 34 continuous attributes. The task is to predict whether the return signal indicates specific physical structures in the ionosphere (good return) or not (bad return). However, the prediction difficulty of two classes is quite different, and ERM was found to achieve a much lower accuracy on bad returns than good ones [33]. In this experiment, both the *training and testing* sets consist of samples with balanced label distribution. But due to the disparity of class difficulty, the prediction accuracy of two classes is quite different, while DRO methods are expected to achieve similar prediction accuracy for both classes. Therefore, in *testing*, we report the testing accuracy for the easy class and the hard class respectively, as well as the AUC score of the testing set. Results are shown in Table 8.

Analysis From the results on real-world data, we find that all DRO methods (WDRO and f-DROs) show significant promotions to ERM, reflecting the reasonability of our experimental settings. And our proposed GDRO outperforms all baselines significantly when dealing with sub-population shifts and class difficulty shifts, which validates the effectiveness of our GDRO.

Table 2: Results of the classification simulated experiment.

	No Label Noises		Add 4% Label Noises	
	$r_1 = 0.5$	$r_2 = 0.0$	$r_1 = 0.5$	$r_2 = 0.0$
ERM	0.573	0.153	0.573	0.152
WDRO	0.576	0.159	0.576	0.157
KL-DRO	0.654	0.340	0.625	0.269
χ^2-DRO	0.734	0.644	0.666	0.554
GDRO	**0.768**	**0.767**	**0.760**	**0.703**

Table 3: Results of Colored MNIST data and Ionosphere data.

Method	Colored MNIST		Ionosphere		
	Train Acc	Test Acc	Easy Class Acc	Hard Class Acc	AUC Score
ERM	0.867	0.116	0.952	0.481	0.683
WDRO	**1.000**	0.335	0.944	0.630	0.774
χ^2-DRO	0.839	0.420	0.976	0.519	0.756
KLDRO	**1.000**	0.287	**0.984**	0.630	0.826
GDRO	0.717	**0.696**	0.962	**0.741**	**0.883**

5 Related Work

Distributionally robust optimization (DRO) directly solves the OOD generalization problem by optimizing the worst-case error in a pre-defined uncertainty set, which is often constrained by moment or support conditions [12, 4], shape constraints [26, 21, 20, 6], f-divergence [27, 15] and Wasserstein distance [31, 34, 5, 16]. [12, 4] set moment or support conditions for the distributions in the uncertainty set. As for shape constraints, one commonly used is unimodality, and [20] uses the orthounimodality to constitute the uncertainty set for DRO for multivariate extreme event analysis. As for f-divergence, [27] theoretically demonstrates that it is equivalent to the variance penalty, and [15] derives the optimization algorithm from its dual reformulation. Compared with f-divergences which require the support of distributions in the uncertainty set is fixed, the uncertainty set built with Wasserstein distance contains distributions with different support and could provide robustness to unseen data. Despite the capacity of a Wasserstein uncertainty set, the optimization of Wasserstein DRO is quite hard. [31, 16, 5] convert the original DRO problem into a regularized ERM problem, but it is suitable only for a limited class of loss functions and transportation cost functions. [34] proposes an approximate optimization method for Wasserstein DRO and could be applied to deep neural networks, which protects the models from adversarial attacks. Besides, DRO methods have also been used for structured data. [22] studies the DRO problem for data generated by a time-homogeneous, ergodic finite-state Markov chain.

Although DRO methods could guarantee the OOD generalization performances when the testing distribution is included in the uncertainty set, there are works [19, 17] doubting their real effects in practice. In order to guarantee the OOD generalization ability, in real scenarios, the uncertainty set has to be overwhelmingly large to contain the potential testing distributions. Such overwhelmingly large set makes the learned model make decisions with fairly low confidence, and it is also referred to as the over-pessimism problem. To mitigate such problem, [17] proposes to incorporate additional unlabeled data to further constrain the uncertainty set, and [24] learns the transportation cost function for WDRO with the help of multiple environment data.

6 Conclusion

Through this work, we take the first step to incorporate data geometry information to mitigate the over-flexibility problem in DRO. In this work, we use the k-nearest-neighbor graph to characterize the data manifold, while our proposed method is compatible with any manifold learning or graph learning methods. And we believe that a more accurate estimated data structure with advanced manifold learning and graph learning algorithms will further boost the performance of GDRO, which we leave for future work.

Acknowledgements

This work was supported in part by National Key R&D Program of China (No. 2018AAA0102004, No. 2020AAA0106300), National Natural Science Foundation of China (No. U1936219, 62141607), Beijing Academy of Artificial Intelligence (BAAI). Bo Li's research was supported by the National Natural Science Foundation of China (No.72171131); the Tsinghua University Initiative Scientific Research Grant (No. 2019THZWJC11); Technology and Innovation Major Project of the Ministry of Science and Technology of China under Grants 2020AAA0108400 and 2020AAA0108403. We would like to thank Yuting Pan, Renzhe Xu, Hao Zou for helpful comments.

A Appendix

A.1 Related Work

Distributionally robust optimization (DRO), stemming from the robust learning literature, directly solves the OOD generalization problem by optimizing the worst-case error in a pre-defined uncertainty set. The choice of the uncertainty set is the key difference of different DRO methods. The uncertainty set is often constrained by moment or support conditions [12, 4], shape constraints [26, 21, 20, 6], f-divergence [27, 15] and Wasserstein distance [31, 34, 5, 16].

[12, 4] set moment or support conditions for the distributions in the uncertainty set. As for shape constraints, one commonly used is unimodality, and [20] uses the orthounimodality to constitute the uncertainty set for DRO for multivariate extreme event analysis. Compared with the shape constraints, our proposed GDRO intrinsically considers the data geometric properties via Geometric Wasserstein distance, and the geometric property is learned in a data-driven way which is compatible with manifold learning and graph learning methods. As for f-DRO, [27] theoretically demonstrates that it is equivalent to the variance penalty, and [15] derives the optimization algorithm from its dual reformulation. Compared with f-divergences which require the support of distributions in the uncertainty set is fixed, the uncertainty set built with Wasserstein distance contains distributions with different support and could provide robustness to unseen data. Despite the capacity of a Wasserstein uncertainty set, the optimization of Wasserstein DRO is quite hard. [31, 16, 5] convert the original DRO problem into a regularized ERM problem, but it is suitable only for a limited class of loss functions and transportation cost functions. [34] proposes an approximate optimization method for Wasserstein DRO and could be applied to deep neural networks, which protects the models from adversarial attacks. Besides, DRO methods have also been used for structured data. For example, [22] studies the DRO problem for data generated by a time-homogeneous, ergodic finite-state Markov chain.

Although DRO methods could guarantee the OOD generalization performances when the testing distribution is included in the uncertainty set, there are works [19, 17] doubting their real effects in practice. In order to guarantee the OOD generalization ability, the uncertainty set should be large enough to capture the potential testing distribution, while in real scenarios, the uncertainty set has to be overwhelmingly large to achieve this. Such overwhelmingly large set makes the learned model make decisions with fairly low confidence, and it is also referred to as the over-pessimism problem. To mitigate such problem, [17] proposes to incorporate additional unlabeled data to further constrain the uncertainty set, and [24] learns the transportation cost function for WDRO with the help of multiple environment data. Different from these works that utilize additional information to constrain the uncertainty set, our proposed GDRO naturally incorporates the data geometric properties into the design of the uncertainty set by firstly using the new distance metric, Geometric Wasserstein distance.

Apart from DRO methods, there are also multiple branches of methods addressing the problem of OOD generalization. Domain generalization methods utilize training data from multiple domains to learn models that generalizes well to unseen domains, and for details of this branch, one can refer to [37]. Invariant learning methods [1], from the causal inference literature, assume the existence of invariant representation and leverage multiple environment data to learn such representations. Compared with DRO methods, they rely on strong assumptions and lack theoretical guarantees.

A.2 Derivations of the Optimization

The whole Forward Euler Method in Section 3.2 is given as:

$$j_{ij} = 1/n(p_i(\ell_j - \ell_i + \beta(\log p_i - \log p_j))_+ - p_j(\ell_j - \ell_i + \beta(\log p_i - \log p_j))_-), \tag{17}$$

$$p_i^{(t+\alpha)} = p_i^{(t)} - \frac{\alpha}{2} \sum_{j:(i,j)\in E} (j_{ij} - j_{ji}) w_{ij}, \tag{18}$$

where $(a)_+ = \max\{a, 0\}$ and $(a)_- = (-a)_+$.

A.3 Proof of Theorem 3.1

Theorem A.1 (Local Robustness Guarantees of Lagrangian Penalty Problem)**.** *For any $t > 0$, $\tau > 0$ and given θ, denote the solution of Equation 5 as $p^*(\theta) = \arg\sup_{p\in\mathscr{P}(G_0)} \mathcal{R}_n(\theta, p) -$*

$\frac{1}{2\tau}\mathcal{GW}^2_{G_0}(\hat{p}^t_\tau(\theta), p)$. *Let* $\epsilon_\tau(\theta) = \mathcal{GW}^2_{G_0}(\hat{p}^t_\tau(\theta), p^*(\theta))$, *we have*

$$\min_{\theta\in\Theta} \sup_{p\in\mathscr{P}_o(G_0)} \mathcal{R}_n(\theta, p) - \frac{1}{2\tau}\mathcal{GW}^2_{G_0}(\hat{p}^t_\tau(\theta), p) = \min_{\theta\in\Theta} \sup_{p:\mathcal{GW}^2_{G_0}(\hat{p}^t_\tau(\theta),p)\le\epsilon_\tau(\theta)} \mathcal{R}_n(\theta, p). \tag{19}$$

Proof. Denote $p^* = \arg\sup_{p\in\mathscr{P}_o(G_0)} \mathcal{R}_n(\theta, p) - \frac{1}{2\tau}\mathcal{GW}^2_{G_0}(\hat{p}^t_\tau, p)$, since $\epsilon_\tau(\theta) = \mathcal{GW}^2_{G_0}(\hat{p}^t_\tau, p^*)$, here we proof by contradiction. Assume $p^{'} = \arg\sup_{p:\mathcal{GW}^2_{G_0}(\hat{p}^t_\tau(\theta),p)\le\epsilon_\tau(\theta)} \mathcal{R}_n(\theta, p)$, then we have $\mathcal{R}(\theta, p^{'}) \ge \mathcal{R}(\theta, p^*)$ and $\mathcal{GW}^2_{G_0}(\hat{p}^t_\tau, p^{'}) \le \epsilon_\tau(\theta)$, and therefore $\mathcal{GW}^2_{G_0}(\hat{p}^t_\tau, p^{'}) \le \mathcal{GW}^2_{G_0}(\hat{p}^t_\tau, p^*)$. Denote $\mathcal{L}(\theta, p) = \mathcal{R}_n(\theta, p) - \frac{1}{2\tau}\mathcal{GW}^2_{G_0}(\hat{p}^t_\tau(\theta), p)$, then we have $\mathcal{L}(\theta, p^*) \le \mathcal{L}(\theta, p^{'})$. Since p^* is the supremum point of $\mathcal{L}(\theta, \cdot)$, it must be $\mathcal{L}(\theta, p^*) = \mathcal{L}(\theta, p^{'})$, which gives that $\mathcal{R}(\theta, p^{'}) = \mathcal{R}(\theta, p^*)$. □

A.4 Proof of Theorem 3.2

The proof is based on the Theorem 5 in [7]. From [7], we have

$$\mathcal{R}(p^\infty) - \mathcal{R}(p(t)) \le e^{-Ct}(\mathcal{R}(p^\infty) - \mathcal{R}(p^0)). \tag{20}$$

Then denote the real worst-case distribution within the $\epsilon(\theta)$-radius discrete Geometric Wasserstein-ball as p^*, that is,

$$p^* = \arg \sup_{p:\mathcal{GW}^2_{G_0}(\hat{P}_{tr},p)\le\epsilon(\theta)} \sum_{i=1}^n p_i\ell_i - \beta\sum_{i=1}^n p_i \log p_i, \tag{21}$$

and we have

$$\mathcal{R}(p^\infty) - \mathcal{R}(p^*) + \mathcal{R}(p^*) - \mathcal{R}(p(t)) \le e^{-Ct}(\mathcal{R}(p^\infty) - \mathcal{R}(p^*) + \mathcal{R}(p^*) - \mathcal{R}(p^0)). \tag{22}$$

Therefore, we have

$$\mathcal{R}(p^*) - \mathcal{R}(p(t)) \le e^{-Ct}(\mathcal{R}(p^*) - \mathcal{R}(p^0)) - (1 - e^{-Ct})(\mathcal{R}(p^\infty) - \mathcal{R}(p^*)), \tag{23}$$

and

$$\frac{\mathcal{R}(p^*) - \mathcal{R}(p(t))}{\mathcal{R}(p^*) - \mathcal{R}(p^0)} \le e^{-Ct} - (1 - e^{-Ct})\frac{\mathcal{R}(p^\infty) - \mathcal{R}(p^*)}{\mathcal{R}(p^*) - \mathcal{R}(p^0)} < e^{-Ct}. \tag{24}$$

(choose $\hat{P}_{tr}$ as p^0).

A.5 Proof of Theorem 3.3

We follow Sinha *et al.*[34] for proof of the convergence properties of our Algorithm. Denote the worst-case distribution as:

$$p^*(\theta) = \arg \max_{p:\mathcal{GW}^2_{G_0}(p,\hat{P}_{tr})\le\hat{\epsilon}(\theta)} \sum_{i=1}^n p_i\ell(f_\theta(x_i), y_i), \tag{25}$$

and our objective function as:

$$F(\theta) = \sum_{i=1}^n p_i^*(\theta)\ell(f_\theta(x_i), y_i), \tag{26}$$

and our learned distribution after k times gradient flow is denoted as p^k. The gradient descent of θ is:

$$\theta^{(t+1)} = \theta^{(t)} - \alpha_t \cdot g^{(t)}, \tag{27}$$

where $g^{(t)} = \nabla_\theta(\sum_{i=1}^n \hat{p}_i^*\ell(f_\theta(x_i), y_i))$ is the gradient approximately calculated under our learned distribution $\hat{p}^*$.

By a Taylor expansion using the L-smoothness of the objective F, we have:

$$F(\theta^{(t+1)}) \le F(\theta^{(t)}) + \langle\nabla_\theta F(\theta^{(t)}), \theta^{(t+1)} - \theta^{(t)}\rangle + \frac{L}{2}\|\theta^{(t+1)} - \theta^{(t)}\|_2^2 \tag{28}$$

$$= F(\theta^{(t)}) - \alpha\langle\nabla_\theta F(\theta^{(t)}), g^{(t)}\rangle + \frac{L\alpha^2}{2}\|g^{(t)}\|_2^2. \tag{29}$$

Then denote the gradient error as:

$$\delta^{(t)} = \nabla_\theta F(\theta^{(t)}) - g^{(t)}, \tag{30}$$

thus, $g^{(t)} = \nabla_\theta F(\theta^{(t)}) - \delta^{(t)}$, and we have:

$$\begin{aligned}
F(\theta^{(t+1)}) &\leq F(\theta^{(t)}) - \alpha\langle\nabla_\theta F(\theta^{(t)}), g^{(t)}\rangle + \frac{L\alpha^2}{2}\|g^{(t)}\|_2^2 && (31)\\
&\leq F(\theta^{(t)}) - \alpha\langle\nabla_\theta F(\theta^{(t)}), \nabla_\theta F(\theta^{(t)}) - \delta^{(t)}\rangle + \frac{L\alpha^2}{2}\|\nabla_\theta F(\theta^{(t)}) - \delta^{(t)}\|_2^2 && (32)\\
&= F(\theta^{(t)}) - \alpha\|\nabla_\theta F(\theta^{(t)})\|_2^2 + \alpha\langle\nabla_\theta F(\theta^{(t)}), \delta^{(t)}\rangle + \frac{L\alpha^2}{2}\|\nabla_\theta F(\theta^{(t)}) - \delta^{(t)}\|_2^2 && (33)\\
&\leq F(\theta^{(t)}) - \frac{\alpha}{2}\|\nabla_\theta F(\theta^{(t)})\|_2^2 + \frac{\alpha}{2}\|\delta^{(t)}\|_2^2 + L\alpha^2\left(\|\nabla_\theta F(\theta^{(t)})\|_2^2 + \|\delta^{(t)}\|_2^2\right) && (34)\\
&= F(\theta^{(t)}) - \frac{\alpha}{2}(1-2L\alpha)\|\nabla_\theta F(\theta^{(t)})\|_2^2 + \frac{\alpha}{2}(1+2L\alpha)\|\delta^{(t)}\|_2^2. && (35)
\end{aligned}$$

Therefore, we have:

$$(1-2L\alpha)\|\nabla_\theta F(\theta^{(t)})\|_2^2 - (1+2L\alpha)\|\delta^{(t)}\|_2^2 \leq \frac{2}{\alpha}\left(F(\theta^{(t)}) - F(\theta^{(t+1)})\right), \tag{36}$$

and average from $t=0$ to K we have:

$$(1-2L\alpha)\frac{1}{K}\sum_{t=1}^{K}\|\nabla_\theta F(\theta^{(t)})\|_2^2 - (1+2L\alpha)\frac{1}{K}\sum_{t=1}^{K}\|\delta^{(t)}\|_2^2 \leq \frac{2}{\alpha K}\left(F(\theta^{(0)}) - F(\theta^{(K+1)})\right), \tag{37}$$

and

$$\frac{1}{K}\sum_{t=1}^{K}\|\nabla_\theta F(\theta^{(t)})\|_2^2 - \frac{(1+2L\alpha)}{1-2L\alpha}\frac{1}{K}\sum_{t=1}^{K}\|\delta^{(t)}\|_2^2 \leq \frac{2}{\alpha K(1-2L\alpha)}\left(F(\theta^{(0)}) - F(\theta^{(K+1)})\right), \tag{38}$$

Take expectations on the both sides like:

$$\frac{1}{K}\mathbb{E}\left[\sum_{t=1}^{K}\|\nabla_\theta F(\theta^{(t)})\|_2^2\right] - \frac{(1+2L\alpha)}{1-2L\alpha}\frac{1}{K}\sum_{t=1}^{K}\|\delta^{(t)}\|_2^2 \leq \frac{2}{\alpha K(1-2L\alpha)}\left(F(\theta^{(0)}) - \mathbb{E}\left[F(\theta^{(K+1)})\right]\right). \tag{39}$$

Then we only have to bound the $\delta^{(t)}$. Following Sinha *et al.*[34], we deal with $\|\delta^{(t)}\|_2^2$. According to the assumption on $R(\theta, p)$, we have

$$\begin{aligned}
\|\delta^{(t)}\|_2^2 = \|\nabla_\theta F(\theta^{(t)}) - g^{(t)}\|_2^2 &= \|\nabla_\theta R(\theta^{(t)}, p^*) - \nabla_\theta R(\theta^{(t)}, \hat{p}^*)\|_2^2 && (40)\\
&\leq L_p^2\|p^* - \hat{p}^*\|_2^2 && (41)\\
&\leq L_p^2\gamma. && (42)
\end{aligned}$$

A.6 Proofs of Theorem 3.4

When relaxing the constrains of ϵ-radius Geometric Wasserstein ball, the objective function becomes:

$$\min_{\theta\in\Theta}\sup_{p\in\mathscr{P}_o(G_0)}\left\{\mathcal{R}_n(\theta, p) = \sum_{i=1}^{n} p_i\ell_i - \beta\sum_{i=1}^{n} p_i\log p_i\right\}, \tag{43}$$

which is equivalent to

$$\min_{\theta\in\Theta}\sup_{p\in\mathscr{P}_o(G_0)}\sum_{i=1}^{n} p_i\ell_i - \beta\cdot\mathrm{D}_{KL}(p\|\hat{P}_{tr}). \tag{44}$$

Then it naturally gives the results in Theorem 3.4 (the proof is similar to Theorem 3.1 and we omit here).

A.7 Relations between GDRO and KL-DRO

Apart from Theorem 3.4, we introduce a more straightforward proposition showing the equivalence of KL-DRO and GDRO as the entropy regularization $\beta \to \infty$.

Proposition A.1 (Reduction of GDRO to KL-DRO)**.** *The objective function of GDRO in Equation (4) is equivalent to the following objective of KL-DRO as $\beta \to \infty$:*

$$\min_{\theta\in\Theta}\left\{G_n^{KL}(\theta) = \sup_{P: D_{KL}(P\|\hat{P}_{tr})\leq\hat{\epsilon}(\theta)} \sum_{i=1}^n p_i\ell(f_\theta(x_i), y_i)\right\}, \quad \textit{with } \hat{\epsilon}(\theta) = D_{KL}(p^*(\theta)\|\hat{P}_{tr}), \tag{45}$$

where $p^*(\theta) = \arg\max_p \sum_{i=1}^n p_i\ell(f_\theta(x_i), y_i) - \beta\sum_{i=1}^n p_i \log p_i$.

Proof. We prove the proposition by showing that both the objectives of GDRO and KL-DRO are reduced to an ERM objective for infinitely large β:

$$\min_{\theta\in\Theta}\left\{G_n^{ERM}(\theta) = \frac{1}{n}\sum_{i=1}^n \ell(f_\theta(x_i), y_i)\right\}. \tag{46}$$

Rewrite the objective of GDRO in Equation (4) as:

$$\min_{\theta\in\Theta}\left\{G_n^{GDRO}(\theta) = \sup_{P:\mathcal{GW}^2_{G_0}(\hat{P}_{tr},P)\leq\epsilon} \sum_{i=1}^n p_i\ell(f_\theta(x_i), y_i) - \beta\sum_{i=1}^n p_i \log p_i\right\}. \tag{47}$$

For any $P \in \mathscr{P}_0(G_0)$ and $P \neq P^U$ where $P^U = (\frac{1}{n}, ..., \frac{1}{n})$ is a uniform distribution, since $\sum_{i=1}^n p_i \log p_i > \sum_{i=1}^n p_i^U \log p_i^U = -\log n$ and $\sum_{i=1}^n p_i\ell(f_\theta(x_i), y_i)$ is bounded w.r.t. P, there exists β_0 such that for any $\beta > \beta_0$:

$$\sum_{i=1}^n p_i\ell(f_\theta(x_i), y_i) - \beta\sum_{i=1}^n p_i \log p_i < \sum_{i=1}^n \frac{1}{n}\ell(f_\theta(x_i), y_i) + \beta\log n. \tag{48}$$

Therefore, as $\beta \to \infty$,

$$\sup_{P:P\in\mathscr{P}_0(G_0)} \sum_{i=1}^n p_i\ell(f_\theta(x_i), y_i) - \beta\sum_{i=1}^n p_i \log p_i = \sum_{i=1}^n \frac{1}{n}\ell(f_\theta(x_i), y_i) + \beta\log n. \tag{49}$$

The supremum is achieved at $P = P^U$. Since P^U satisfies $\mathcal{GW}^2_{G_0}(\hat{P}_{tr}, P) = 0 \leq \epsilon$ for any positive ϵ, the objective of GDRO is reduced to:

$$G_n^{GDRO}(\theta) = \frac{1}{n}\sum_{i=1}^n \ell(f_\theta(x_i), y_i) + \beta\log n, \quad \text{as } \beta \to \infty, \tag{50}$$

which is equivalent as G_n^{ERM} except for a constant independent of θ.

Next, the objective of KL-DRO $G_n^{KL}(\theta)$ could be similarly reformulated as is in the proof of Theorem 3.1:

$$G_n^{KL}(\theta) = \sup_{P:P\in\mathscr{P}_o(G_0)} \sum_{i=1}^n p_i\ell(f_\theta(x_i), y_i) - \beta\sum_{i=1}^n p_i \log p_i. \tag{51}$$

According to Equation 49, as $\beta \to \infty$,

$$G_n^{KL}(\theta) = \sum_{i=1}^n \frac{1}{n}\ell(f_\theta(x_i), y_i) + \beta\log n = G_n^{GDRO}(\theta). \tag{52}$$

□

A.8 Limitations

GDRO handles unseen inside-manifold distributions with various categories of shifts as is stated in the experiment section, including sub-population shifts and class difficulty shifts. However, generalization to target data entirely falling out of the training data's manifold, known as support shift or non-overlapping support, is intrinsically a hard problem. In standard supervised learning, covariate shift with arbitrary support is known to be intractable [3]. Some domain adaptation methods, such as invariant representation learning [39], could empirically validate its effectiveness out of support while still requiring the target distribution to be close to the source's. Not to mention that such methods have utilized unlabeled target data from the unseen support. Therefore, out-of-support generalization is not the focus of GDRO for lack of additional information and strong structural assumptions. And we leave it to future work.

B Experiments

In this section, we introduce the details of our experiments.

Dataset Summary In order to comprehensively evaluate the empirical performance of our proposed GDRO, we experiment on both simulated and real-world datasets with various distributional shift patterns studied by OOD generalization, including sub-population shifts and label shifts. The descriptions of our adopted datasets are shown in Table 4.

Table 4: Datasets descriptions.

Dataset	Toy Example	Manifold	Selection Bias	Colored MNIST	Retiring Adults	HIV	IonoSphere
Kind	Regression	Classification	Regression	Classification	Classification	Classification	Classification
Data Generation	Simulation	Simulation	Simulation	Real	Real	Real	Real
Dimension.	2	300	10	2352	10∼19	160	34
Shift Pattern	Sub-population	Domain Shift	Domain Shift	Domain Shift	Sub-population	Label Shift	Label Shift
Model	Linear	Linear	Linear	MLP	Linear	MLP	MLP

Baselines We compare our GDRO with the following baselines:

- Empirical Risk Minimization (ERM):

$$\min_{\theta} \frac{1}{N} \sum_{i=1}^{N} \ell(y_i, f_\theta(x_i)). \tag{53}$$

- Wasserstein DRO (WDRO [5, 34]):

$$\min_{\theta} \sup_{Q: W_c(Q, \hat{P}_N) \leq \epsilon} \mathbb{E}_Q[\ell(Y, f_\theta(X))]. \tag{54}$$

- KL-DRO [15]:

$$\min_{\theta} \sup_{q: \mathrm{D}_{KL}(q \| \hat{P}_N) \leq \epsilon} \sum_{i=1}^{N} q_i \ell(y_i, f_\theta(x_i)). \tag{55}$$

- χ^2-DRO [27, 15]:

$$\min_{\theta} \sup_{q: \mathrm{D}_{\chi^2}(q, \hat{P}_N) \leq \epsilon} \sum_{i=1}^{N} q_i \ell(y_i, f_\theta(x_i)). \tag{56}$$

- Environment Inference for Invariant Learning (EIIL [8]): this method belongs to invariant learning. As a general OOD generalization method from another branch, we temporarily add it only in the Colored MNIST experiment.

Implementation Details For all experiments, G_0 is constructed as a k-nearest neighbor graph from the *training data only* at the initialization step. Specifically, we adopt NN-Descent to estimate the k-nearest neighbor graph for the large-scale dataset Colored MNIST while performing exact search for k-nearest neighbors in other experiments. We adopt MSE as the empirical loss function for regression tasks and cross-entropy for classification tasks. The parameterized model f_θ is implemented as

a MLP with a hidden layer of 64 neurons for the HIV and IonoSphere dataset, a MLP with two hidden layers of 128 neurons for Colored MNIST, and a linear model in the other experiments. Note that GDRO is *compatible with any parameterized models including DNN*. The training of MLP is performed with a batch size of 1024 and a learning rate at 0.001. The simulation of gradient flow in Equation 17-18 is implemented by message propagation with DGL package [38], which scales linearly with sample size and enjoys parallelization by GPU.

B.1 Simulation Data

As for the simulation data, we simulate domain shifts between training data and testing data for both regression and classification settings. And we also investigate the influence brought by label noises to demonstrate that our GDRO could to some extent resist label noise.

1. Toy Example: Sub-population Shifts via Anti-Causal Effect

Firstly, inspired by [1], we induce the domain shifts via the anti-causal effect as follows:

$$S \sim \mathcal{N}(0,1), \quad Y = \alpha_S S + S^2 + \mathcal{N}(0,0.1), \quad V = \alpha_V Y + \mathcal{N}(0,1), \quad \alpha_V = \begin{cases} 1 & \textit{with probability } 1-r, \\ -0.1 & \textit{with probability } r, \end{cases} \tag{57}$$

where $X = [S, V]^T$, S serves as a stable feature with an unchanged relationship with Y (thus it should be used for prediction), but V is a spurious feature with changeable relationships with Y (thus one should avoid using it), and α_S is set to 5.0 for all data. For training data, we sample 10000 points, and design different settings with varying minor group ratios r. For testing data, we simulate 6 domains with strong shifts by varying $\alpha_V \in \{-3, -2, -1, 1, 2, 3\}$ ($V = \alpha_V Y + \mathcal{N}(0,1)$) and calculate the Mean_Error, Std_Error and parameter estimation error Est_Error for each method as:

- Mean Error: Mean_Error $= \frac{1}{|\mathcal{E}_{test}|} \sum_e \mathcal{L}^e$
- Standard Deviation of Error: Std_Error $= \sqrt{\frac{1}{|\mathcal{E}_{test}|-1} \sum_e (\mathcal{L}^e - \text{Mean\_Error})^2}$
- Parameter Estimation Error: Est_Error $= |\hat{\alpha}_S - \alpha_S| + |\hat{\alpha}_V|$, where $\hat{\alpha}_S$, $\hat{\alpha}_V$ denote the estimated parameters for S and V respectively. Note that the ground-truth α_V is 0.

Analysis From the results in Table 5, WDRO performs similarly to ERM, and two f-DRO methods (KL-DRO and χ^2-DRO) outperform ERM and WDRO. Such results verify our analysis that the Wasserstein uncertainty set cannot be large due to its over-flexibility, which greatly impairs its performance under strong domain shifts. Our GDRO outperforms all baselines and achieves much lower prediction errors and estimation errors in all settings, which shows our uncertainty set built on Geometric Wasserstein distance is much more practical and reasonable. Further, we plot the training data in Figure 8. From Figure 8, we can see that although the training data is low-dimensional, they have geometric structures, which are utilized by our GDRO to achieve good OOD generalization performances.

2. High-dimensional Data with Low-dimensional Structure: Sub-population Shifts

In this setting, data are high-dimensional but with low-dimensional structure. The data generation is similar to [30] and is a typical classification setting in OOD generalization. We introduce the spurious correlation between the label $Y = \{+1, -1\}$ and the spurious attribute $A = \{+1, -1\}$. We firstly generate low-dimensional data $X_{low} = [S, V]^T \in \mathbb{R}^{10}$ as:

$$S \sim \mathcal{N}(Y\mathbf{1}, \sigma_s^2 \mathbb{I}_5), V \sim \mathcal{N}(A\mathbf{1}, \sigma_v^2 \mathbb{I}_5), \tag{58}$$

Table 5: Results of the toy example with varying minor probability r. Each result is averaged over 10 runs, and the standard deviation is omitted since it is small for all methods.

Simulation 1: Toy Example (Domain Shift via Anti-Causal Effect)									
Minor Probability	$r = 0.01$			$r = 0.05$			$r = 0.1$		
	Mean_Error	Std_Error	Est_Error	Mean_Error	Std_Error	Est_Error	Mean_Error	Std_Error	Est_Error
ERM	7.144	4.260	3.999	5.594	3.210	2.970	4.521	2.444	2.230
WDRO	5.396	3.480	3.024	4.303	2.656	2.297	3.451	1.974	1.700
KL-DRO	2.672	1.145	1.134	2.678	1.148	1.194	2.531	1.086	1.157
χ^2-DRO	3.027	1.323	1.185	2.954	1.262	1.118	2.738	1.079	0.953
GDRO	**1.759**	**0.047**	**0.287**	**1.718**	**0.066**	**0.043**	**1.769**	**0.153**	**0.072**

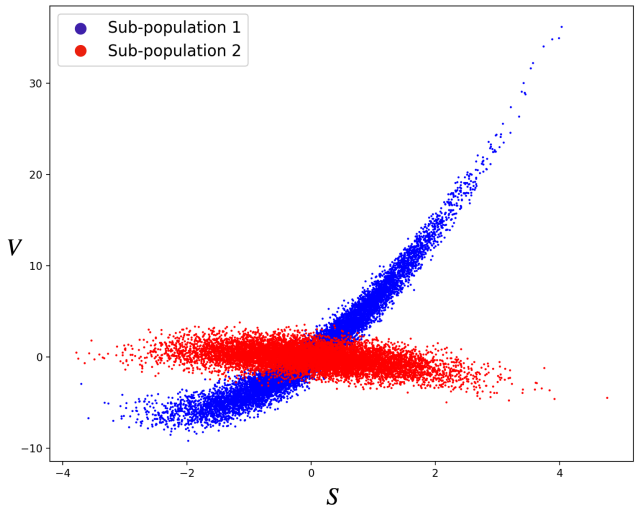

Figure 4: Data distribution of the toy example with $r = 0.5$ (the two sub-populations are balanced).

Table 6: The testing accuracy over 10 runs for the simulated experiments on high-dimensional data.

	No Label Noises		Add 4% Label Noises	
	$r_1 = 0.5$	$r_2 = 0.0$	$r_1 = 0.5$	$r_2 = 0.0$
ERM	0.573	0.153	0.573	0.152
WDRO	0.576	0.159	0.576	0.157
KL-DRO	0.654	0.340	0.625	0.269
χ^2-DRO	0.734	0.644	0.666	0.554
GDRO	**0.768**	**0.767**	**0.760**	**0.703**

and

$$A = \begin{cases} Y, \text{with probability } r, \\ -Y, \text{with probability } 1-r. \end{cases} \tag{59}$$

Intuitively, $r \in [0, 1]$ controls the spurious correlation between A and Y. When $r > 0.5$, the spurious attribute A is positively correlated with Y, and when $r < 0.5$, the spurious correlation becomes negative. And larger $|r - 0.5|$ results in stronger spurious correlation between A and Y.

Then to convert the low-dimensional data to high-dimensional space, X_{low} is multiplied by a column full rank matrix H as:

$$X_{high} = (HX_{low}) \in \mathbb{R}^{300}, \tag{60}$$

where $H \in \mathbb{R}^{300\times 10}$ and each column of H is linearly independent from each other (H is full column rank). We randomly choose such H in each run to introduce some randomness.

For the both training and testing data, we set $\sigma_s^2 = 1.0$ and $\sigma_v^2 = 0.3$. In training, we set $r = 0.85$ (A is positively correlated with Y). In testing, we design two environments with $r_1 = 0.5$ ($A \perp Y$) and $r_2 = 0.0$ (A is negatively correlated with Y) to introduce distributional shifts.

Apart from the natural setting without label noises, we also test the performances under label noises. Specifically, we add 4% label noises in the training data by flipping the label Y. We run the experiments for 10 times, and each time with one random matrix H. The results over 10 runs are shown in Table 6.

3. Selection Bias: Domain Shift via Selection Bias Mechanism

Secondly, a more complicated mechanism is designed via selection bias as:

$$S \sim \mathcal{N}(0, 2\mathbb{I}_{n_s}) \in \mathbb{R}^5, \;\; V \sim \mathcal{N}(0, 2\mathbb{I}_{n_v}) \in \mathbb{R}^5, \;\; Y = \beta^T S + 0.1 \cdot S_1 S_2 S_3 + \mathcal{N}(0, 0.5). \tag{61}$$

Similar to the toy example above, S are stable features while the relationships between V and Y are perturbed in different domains. Specifically, a data point is selected with probability $P(x_i, y_i) = |r|^{-5*|y_i - \text{sign}(r)\cdot v_i^b|}$, which induces the spurious correlation between a certain covariate $V^b \in V$ and

Y. In training, we generate 10000 points, where the major group contains 95% data with $r = 1.9$ and the minor group contains 5% data with $r = -1.3$. In testing, we first report the performances of the two training groups, and then we further vary $r \in \{-1.5, -1.7, -1.9, -2.3, -2.7, -3.0\}$ to simulate more challenging domain shifts that cannot be obtained by interpolation between training groups. The average results over ten runs are shown in Table 7 (simulation 2). As for sub-population shifts, GDRO achieves good tail performance at a slight sacrifice of the performance of the major group. Further, for more challenging domain shifts, GDRO significantly outperforms all baselines in all testing distributions, even though the shifts are much stronger than the training.

Table 7: Results on the Selection Bias Experiments. We report the root mean square errors.

Simulation 2: Selection Bias Experiment without Label Noises									
	Train(major)	Train(minor)	Test						Parameter
Bias Ratio r	$r = 1.9$	$r = -1.3$	$r = -1.5$	$r = -1.7$	$r = -1.9$	$r = -2.3$	$r = -2.7$	$r = -3.0$	Est_ Error
ERM	**0.339**	0.876	0.892	0.884	0.864	0.880	0.843	0.888	0.423
WDRO	**0.339**	0.877	0.894	0.885	0.865	0.882	0.844	0.890	0.424
χ^2-DRO	0.411	0.744	0.757	0.741	0.733	0.742	0.714	0.755	0.367
KL-DRO	0.370	0.713	0.728	0.716	0.708	0.713	0.685	0.724	0.319
GDRO	0.493	**0.492**	**0.508**	**0.489**	**0.501**	**0.483**	**0.486**	**0.496**	**0.033**
Simulation 3: Selection Bias Experiment under Label Noises									
ERM	**0.335**	0.845	0.885	0.879	0.874	0.884	0.882	0.876	0.422
WDRO	**0.335**	0.896	0.887	0.880	0.875	0.886	0.884	0.877	0.423
χ^2-DRO	0.375	0.866	0.855	0.856	0.843	0.860	0.854	0.845	0.408
KL-DRO	0.393	0.879	0.868	0.866	0.856	0.876	0.866	0.861	0.391
GDRO	0.542	**0.537**	**0.553**	**0.549**	**0.534**	**0.539**	**0.555**	**0.550**	**0.058**

3. Label Noises: Add Label Noises

Since DRO methods are risk-aware, they are prone to be affected by label noises. Though the effect of label noises cannot be eliminated due to the nature of DRO, our proposed GDRO could significantly improve the resistance of DRO methods to a minor degree of label noises. Based on the selection bias experiment, we random sample 20 points and add label noises on them via $\tilde{Y} = Y + \text{Std}(Y)$ where $\text{std}(Y)$ denotes the standard derivation of the marginal distribution of Y. From results shown in Table 7(simulation 3), both f-DRO methods are significantly affected and perform similarly to ERM under such a minor degree of label noises. And our GDRO is only slightly affected by the label noises.

Further, to demonstrate the difference between f-DRO, WDRO, and GDRO, for the label noise experiment, we visualize the learned worst-case distribution of three methods. **(1)** In the first two figures in Figure 5(a), we draw the learned sample weights of KL-DRO and GDRO, where red points represent the noisy samples in training data, and the size of each point is proportional to its sample weight. We can see that KL-DRO puts heavy weights on the noisy points (the red nodes are much larger), while our GDRO only slightly increases them and the weights of data in the minor group are raised, which results in the difference between their performances in the label noise experiment. The reason for such phenomenon of KL-DRO is that it ignores the data geometry, allowing for some isolated nodes with much heavier weights than surrounding nodes, which corresponds with our Theorem 3.4. Since our GDRO intrinsically naturally constrains weight learning on the data manifold, the learned weights are smooth w.r.t the data manifold. **(2)** In the third figure in Figure 5(a), the red points represent the samples, to which WDRO introduces label noises with the ratio larger than 50%, and the size of each point is proportional to its label noise ratio. We can see that although WDRO extends the support, the created samples are quite noisy and greatly harm the learning process. **(3)** To quantify this property, we measure the smoothness via Dirichlet Energy and plot the Dirichlet Energy w.r.t the relative entropy $KL(p\|\hat{P}_{tr})$ between the learned distribution and training distribution in Figure 5(b), which shows that the learned weights of GDRO are much more smooth on the data manifold than that of KL-DRO.

B.2 Real-World Data

Finally, towards a comprehensive comparison with existing DRO methods, we evaluate our method on four real-world datasets with various kinds of distributional shifts, including sub-population shifts, domain shifts, class-wise shifts, and label noises. All experimental details can be found in Appendix.

1. Retiring Adults: Sub-population Shifts The Retiring Adults dataset [13] is derived from US Census surveys, where the sub-population shifts are natural since there are geographic variations across different states. Our experiments involve three prediction tasks defined in [13], including

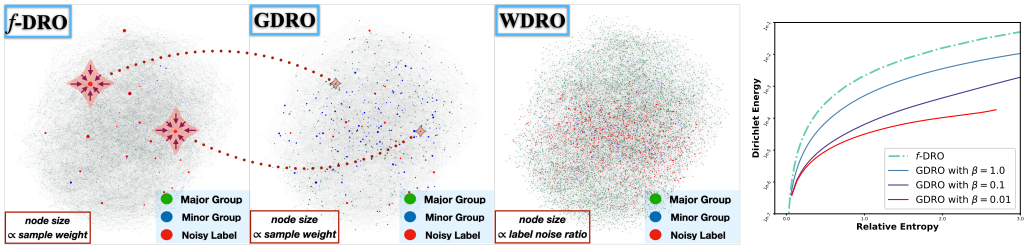

(a) Visualization of learned weights of f-DRO and GDRO. (b) Weight smoothness.

Figure 5: Explanatory studies for comparison between f-DRO ($f(x) = x \ln x$) and GDRO. **Figure (a)** visualizes the learned worst-case distribution of f-DRO, GDRO, and WDRO on kNN, and the size of each node is proportional to its sample weight or its label noise ratio. **Figure (b)** plots the Dirichlet Energy w.r.t the relative entropy, which measures the smoothness of learned weights given the same $D_{KL}(p\|\hat{P}_{tr})$.

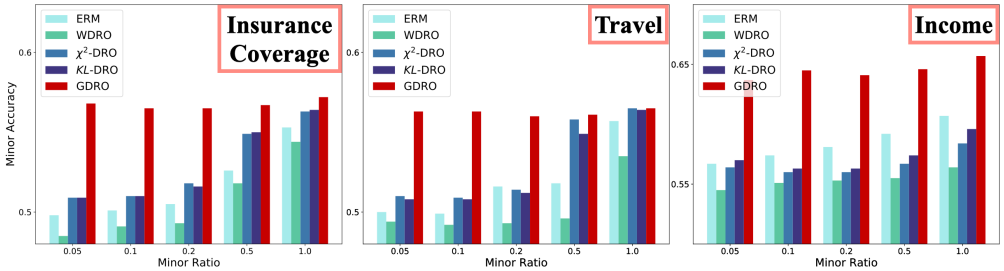

(a) Health Insurance Coverage Data. **(b) Travel Time Data.** **(c) People Income Data.**

Figure 6: Results of Retiring Adults Dataset.

Income Prediction, Public Health Insurance Coverage Prediction, and Commuting Time Prediction. For each task, we randomly sample 2000 points from state A and $2000 \cdot r$ points from state B, where $r < 1$ and the second state is viewed as the minor group. In Figure 6, we report the prediction accuracy of the minor group for different minority ratios r in three tasks.

2. HIV-1: Sub-population Shifts & Label Imbalance HIV-1 Protease Cleavage Dataset [10] involves a task to predict whether an octamer would be cleaved by HIV-1 protease, given a 160-dimensional one-hot vector encoding the sequence of 8 amino acids composing the octamer. The dataset contains 4 splits, and following [28], we merge '746' and '1625' as subpopulations A and view 'Impens' as B. In training, subpopulations A and B are mixed at a ratio of $1 : r$, where $r \leq 1$ is the minor group ratio. Coupled with the sub-population shift, class labels are imbalanced with 33% positive in sub-population A and 16% positive in B, which is more challenging. In testing, we re-balance the two classes and plot the overall accuracy w.r.t. the minor group ratio in Figure 7.

3. Colored MNSIT: Domain Shifts & Label Noises Following Arjovsky *et al.* [1], we conduct a binary classification task on the MNIST dataset. Firstly, a binary label Y is assigned to each image according to its digit: $Y = 0$ for digit $0 \sim 4$ and $Y = 1$ for digit $5 \sim 9$. Secondly, we induce noisy labels $\tilde{Y}$ by randomly flipping the label Y with a probability of 0.2. Then we induce domain shifts by sampling the color id C spuriously correlated with $\tilde{Y}$. Specifically, we generate C by flipping $\tilde{Y}$ with probability r, which can be viewed as the indicator of different domains. In training, we randomly sample 5000 data points and set $r = 0.85$ and in testing, we set $r = 0$, which induces strong domain shifts between training and testing. Results are shown in Table 8.

4. Ionosphere Radar Classification: Class Difficulty Shifts Ionosphere Radar Dataset [11] consists of return signals from the ionosphere of a phased array radar system in Google Bay, Labrador. The electromagnetic signals were processed by an auto-correlation function to produce 34 continuous attributes. The target is to determine whether the return signal indicates specific physical structures in the ionosphere (good return) or not (bad return). Due to the disparity between classes, ERM was found to achieve a much lower accuracy on bad returns than good ones [33]. DRO methods are expected to achieve higher accuracy in the harder class. Results are shown in Table 8.

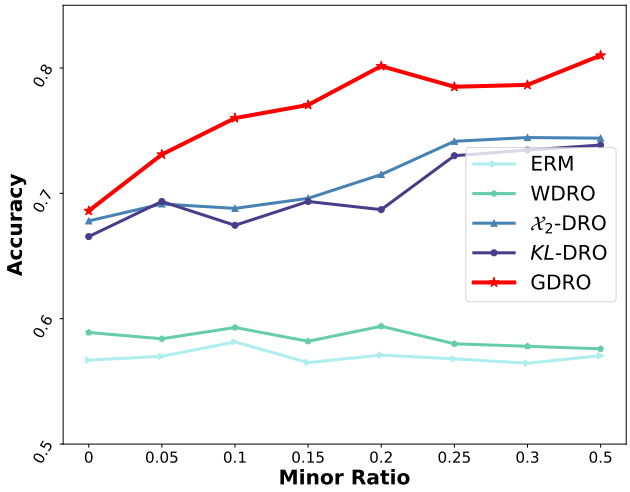

Figure 7: Results of the HIV-1 data.

Table 8: Results of Colored MNIST data and Ionosphere data.

Method	Colored MNIST		Ionosphere		
	Train Acc	Test Acc	Easy Class Acc	Hard Class Acc	AUC Score
ERM	0.867	0.116	0.952	0.481	0.683
WDRO	**1.000**	0.335	0.944	0.630	0.774
χ^2-DRO	0.839	0.420	0.976	0.519	0.756
KLDRO	**1.000**	0.287	**0.984**	0.630	0.826
EIIL	0.740	0.596	-	-	-
GDRO	0.717	**0.696**	0.962	**0.741**	**0.883**

Analysis From the results on real-world data, we find that in most scenarios, WDRO only slightly outperforms ERM, and two f-DRO methods show significant promotions to ERM. Our proposed GDRO outperforms all baselines significantly in all scenarios. (1) The discrepancy between WDRO ($\approx$ ERM) and f-DRO ($>$ ERM) indicates that the extending the distribution support in practice is not as promising as might be expected, which we think is because creating new data points is nearly impossible in real scenarios. (2) The significant discrepancy between GDRO ($\gg$ ERM) and WDRO ($\approx$ ERM) shows the superiority of restricting the distribution support, which enables DRO to provide robustness in a much larger uncertainty set without worrying about generating unrealistic samples. (3) GDRO exhibits significant advantages under strong distributional shifts (small minor ratio in Figure 6 and Figure 7; strong shifts in Colored MNSIT in Table 8), which shows that by incorporating geometric properties, our uncertainty set mitigates the over-flexibility problem and our GDRO can resist stronger distributional shifts.

B.3 Supplementary Figures

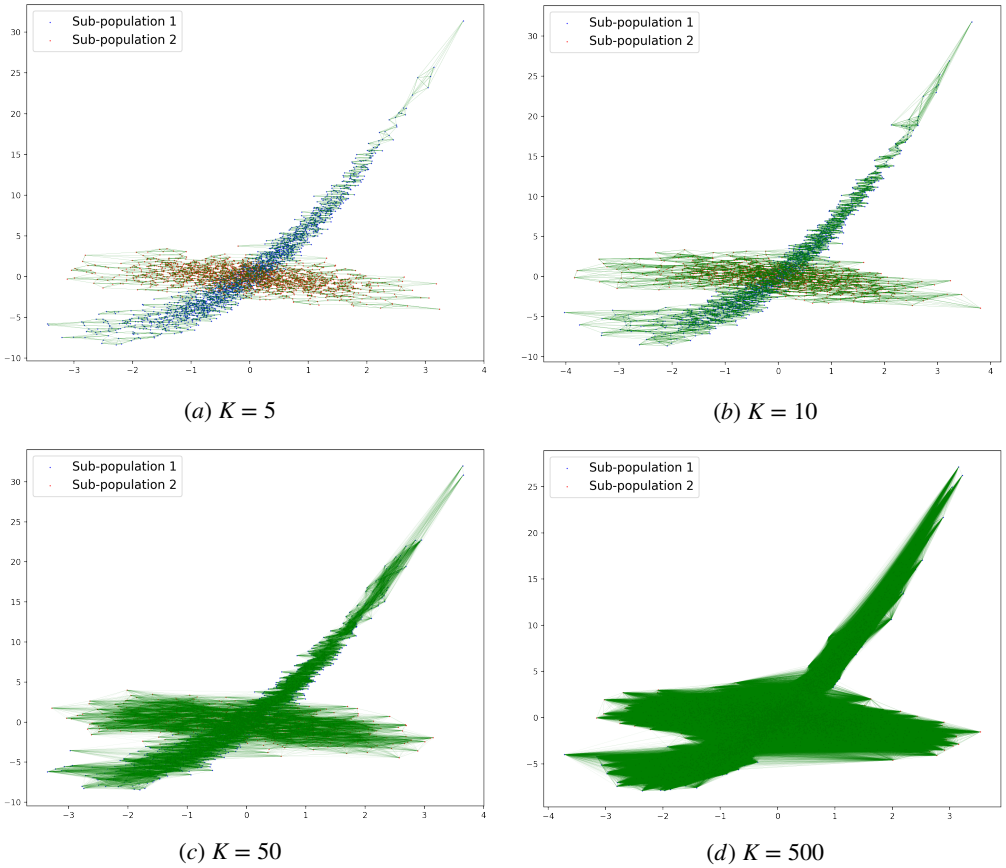

(a) $K = 5$ (b) $K = 10$

(c) $K = 50$ (d) $K = 500$

Figure 8: KNN graphs for Toy Example under various values of K.

References

[1] Martin Arjovsky, Léon Bottou, Ishaan Gulrajani, and David Lopez-Paz. Invariant risk minimization. *arXiv preprint arXiv:1907.02893*, 2019.

[2] Mikhail Belkin and Partha Niyogi. Laplacian eigenmaps for dimensionality reduction and data representation. *Neural computation*, 15(6):1373–1396, 2003.

[3] Shai Ben-David, Tyler Lu, Teresa Luu, and Dávid Pál. Impossibility theorems for domain adaptation. In Yee Whye Teh and D. Mike Titterington, editors, *Proceedings of the Thirteenth International Conference on Artificial Intelligence and Statistics, AISTATS 2010, Chia Laguna Resort, Sardinia, Italy, May 13-15, 2010*, volume 9 of *JMLR Proceedings*, pages 129–136. JMLR.org, 2010.

[4] Dimitris Bertsimas, Vishal Gupta, and Nathan Kallus. Data-driven robust optimization. *Mathematical Programming*, 167(2):235–292, 2018.

[5] Ruidi Chen and Ioannis C Paschalidis. A robust learning approach for regression models based on distributionally robust optimization. *Journal of Machine Learning Research*, 19(13), 2018.

[6] Xi Chen, Simai He, Bo Jiang, Christopher Thomas Ryan, and Teng Zhang. The discrete moment problem with nonconvex shape constraints. *Operations Research*, 69(1):279–296, 2021.

[7] Shui-Nee Chow, Wuchen Li, and Haomin Zhou. Entropy dissipation of fokker-planck equations on graphs. *arXiv preprint arXiv:1701.04841*, 2017.

[8] Elliot Creager, Jörn-Henrik Jacobsen, and Richard Zemel. Environment inference for invariant learning. In *International Conference on Machine Learning*, pages 2189–2200. PMLR, 2021.

[9] Emma Dann, Neil C Henderson, Sarah A Teichmann, Michael D Morgan, and John C Marioni. Differential abundance testing on single-cell data using k-nearest neighbor graphs. *Nature Biotechnology*, 40(2):245–253, 2022.

[10] HIV-1 Protease Cleavage Dataset. https://archive-beta.ics.uci.edu/ml/datasets/hiv+1+protease +cleavage. 2015.

[11] Ionosphere Radar Dataset. https://archive-beta.ics.uci.edu/ml/datasets/ionosphere.

[12] Erick Delage and Yinyu Ye. Distributionally robust optimization under moment uncertainty with application to data-driven problems. *Operations research*, 58(3):595–612, 2010.

[13] Frances Ding, Moritz Hardt, John Miller, and Ludwig Schmidt. Retiring adult: New datasets for fair machine learning. *Advances in Neural Information Processing Systems*, 34, 2021.

[14] Wei Dong, Moses Charikar, and Kai Li. Efficient k-nearest neighbor graph construction for generic similarity measures. In Sadagopan Srinivasan, Krithi Ramamritham, Arun Kumar, M. P. Ravindra, Elisa Bertino, and Ravi Kumar, editors, *Proceedings of the 20th International Conference on World Wide Web, WWW 2011, Hyderabad, India, March 28 - April 1, 2011*, pages 577–586. ACM, 2011.

[15] John C Duchi and Hongseok Namkoong. Learning models with uniform performance via distributionally robust optimization. *The Annals of Statistics*, 49(3):1378–1406, 2021.

[16] Peyman Mohajerin Esfahani and Daniel Kuhn. Data-driven distributionally robust optimization using the wasserstein metric: performance guarantees and tractable reformulations. *Math. Program.*, 171(1-2):115–166, 2018.

[17] Charlie Frogner, Sebastian Claici, Edward Chien, and Justin Solomon. Incorporating unlabeled data into distributionally robust learning. *arXiv preprint arXiv:1912.07729*, 2019.

[18] Jens Hainmueller. Entropy balancing for causal effects: A multivariate reweighting method to produce balanced samples in observational studies. *Political analysis*, 20(1):25–46, 2012.

[19] Weihua Hu, Gang Niu, Issei Sato, and Masashi Sugiyama. Does distributionally robust supervised learning give robust classifiers? In *International Conference on Machine Learning*, pages 2029–2037. PMLR, 2018.

[20] Henry Lam, Zhenyuan Liu, and Xinyu Zhang. Orthounimodal distributionally robust optimization: Representation, computation and multivariate extreme event applications. *arXiv preprint arXiv:2111.07894*, 2021.

[21] Henry Lam and Clementine Mottet. Tail analysis without parametric models: A worst-case perspective. *Operations Research*, 65(6):1696–1711, 2017.

[22] Mengmeng Li, Tobias Sutter, and Daniel Kuhn. Distributionally robust optimization with markovian data. In Marina Meila and Tong Zhang, editors, *Proceedings of the 38th International Conference on Machine Learning, ICML 2021, 18-24 July 2021, Virtual Event*, volume 139 of *Proceedings of Machine Learning Research*, pages 6493–6503. PMLR, 2021.

[23] Evan Z Liu, Behzad Haghgoo, Annie S Chen, Aditi Raghunathan, Pang Wei Koh, Shiori Sagawa, Percy Liang, and Chelsea Finn. Just train twice: Improving group robustness without training group information. In *International Conference on Machine Learning*, pages 6781–6792. PMLR, 2021.

[24] Jiashuo Liu, Zheyan Shen, Peng Cui, Linjun Zhou, Kun Kuang, Bo Li, and Yishi Lin. Stable adversarial learning under distributional shifts. In *Proceedings of the AAAI Conference on Artificial Intelligence*, volume 35, pages 8662–8670, 2021.

[25] Leland McInnes, John Healy, and James Melville. Umap: Uniform manifold approximation and projection for dimension reduction. *arXiv preprint arXiv:1802.03426*, 2018.

[26] Clementine Mottet and Henry Lam. On optimization over tail distributions. *arXiv preprint arXiv:1711.00573*, 2017.

[27] Hongseok Namkoong and John C Duchi. Variance-based regularization with convex objectives. *Advances in neural information processing systems*, 30, 2017.

[28] Thorsteinn S. Rögnvaldsson, Liwen You, and Daniel Garwicz. State of the art prediction of HIV-1 protease cleavage sites. *Bioinform.*, 31(8):1204–1210, 2015.

[29] Sam T Roweis and Lawrence K Saul. Nonlinear dimensionality reduction by locally linear embedding. *science*, 290(5500):2323–2326, 2000.

[30] Shiori Sagawa, Aditi Raghunathan, Pang Wei Koh, and Percy Liang. An investigation of why overparameterization exacerbates spurious correlations. In *International Conference on Machine Learning*, pages 8346–8356. PMLR, 2020.

[31] Soroosh Shafieezadeh-Abadeh, Peyman Mohajerin Esfahani, and Daniel Kuhn. Distributionally robust logistic regression. In Corinna Cortes, Neil D. Lawrence, Daniel D. Lee, Masashi Sugiyama, and Roman Garnett, editors, *Advances in Neural Information Processing Systems 28: Annual Conference on Neural Information Processing Systems 2015, December 7-12, 2015, Montreal, Quebec, Canada*, pages 1576–1584, 2015.

[32] Soroosh Shafieezadeh Abadeh, Peyman M Mohajerin Esfahani, and Daniel Kuhn. Distributionally robust logistic regression. *Advances in Neural Information Processing Systems*, 28, 2015.

[33] Vincent G Sigillito, Simon P Wing, Larrie V Hutton, and Kile B Baker. Classification of radar returns from the ionosphere using neural networks. *Johns Hopkins APL Technical Digest*, 10(3):262–266, 1989.

[34] Aman Sinha, Hongseok Namkoong, Riccardo Volpi, and John Duchi. Certifying some distributional robustness with principled adversarial training. *arXiv preprint arXiv:1710.10571*, 2017.

[35] Joshua B Tenenbaum, Vin de Silva, and John C Langford. A global geometric framework for nonlinear dimensionality reduction. *science*, 290(5500):2319–2323, 2000.

[36] Cédric Villani. Topics in optimal transportation. 58, 2021.

[37] Jindong Wang, Cuiling Lan, Chang Liu, Yidong Ouyang, Tao Qin, Wang Lu, Yiqiang Chen, Wenjun Zeng, and Philip Yu. Generalizing to unseen domains: A survey on domain generalization. *IEEE Transactions on Knowledge and Data Engineering*, 2022.

[38] Minjie Wang, Da Zheng, Zihao Ye, Quan Gan, Mufei Li, Xiang Song, Jinjing Zhou, Chao Ma, Lingfan Yu, Yu Gai, Tianjun Xiao, Tong He, George Karypis, Jinyang Li, and Zheng Zhang. Deep graph library: A graph-centric, highly-performant package for graph neural networks. *arXiv preprint arXiv:1909.01315*, 2019.

[39] Han Zhao, Remi Tachet des Combes, Kun Zhang, and Geoffrey J. Gordon. On learning invariant representations for domain adaptation. In Kamalika Chaudhuri and Ruslan Salakhutdinov, editors, *Proceedings of the 36th International Conference on Machine Learning, ICML 2019, 9-15 June 2019, Long Beach, California, USA*, volume 97 of *Proceedings of Machine Learning Research*, pages 7523–7532. PMLR, 2019.